Robust Adaptive Detection of Buried Pipes using GPR

Q Hoarau, G Ginolhac, A Atto, J M Nicolas

Robust Adaptive Detection of Buried Pipes using GPR

Q. Hoarau, G. Ginolhac, A. M. Atto, J.M. Nicolas[1]

LISTIC, Université de Savoie Mont-Blanc, B.P. 80439 74944 Annecy le Vieux Cedex, France

LTCI, Telecom ParisTech, 46 Rue Barrault, F-75634 Paris Cedex 13, France

Abstract

Detection of buried objects such as pipes using a Ground Penetrating Radar (GPR) is intricate for three main reasons. First, noise is important in the resulting image because of the presence of several rocks and/or layers in the ground, highly influencing the Probability of False Alarm (PFA) level. Also, wave speed and object responses are unknown in the ground and depend on the relative permittivity, which is not directly measurable. Finally, the depth of the pipes leads to strong attenuation of the echoed signal, leading to poor SNR scenarios. In this paper, we propose a detection method: (1) enhancing the signal of interest while reducing the noise and layer contributions, and (2) giving a local estimate of the relative permittivity. We derive an adaptive detector where the signal of interest is parametrised by the wave speed in the ground. For this detector, noise is assumed to follow a Spherically Invariant Random Vector (SIRV) distribution in order to obtain a robust detection. We use robust maximum likelihood-type covariance matrix estimators called *M-estimators*. To handle the significant amount of data, we consider regularised versions of said estimators. Simulation will allow to estimate the relation PFA-Threshold. Comparison is performed with standard GPR processing methods, showing the aptitude of the method in detecting pipes having low response levels with a reasonable PFA.

Keywords: GPR, buried pipes, adaptive detection, covariance matrix, non Gaussian, regularised covariance matrix estimator.

Email address:
quentin.hoarau,guillaume.ginolhac,abdourrahmane.atto@univ-smb.fr,
jean-marie.nicolas@telecom-paristech.fr (Q. Hoarau, G. Ginolhac, A. M. Atto, J.M. Nicolas)

1. Introduction

Ground Penetrating Radar (GPR) imaging involves transmitting an electromagnetic wave at several spatial positions and receiving subsoil retro-diffusion waves to form images [1, 2]. In particular, GPR can be used to detect buried objects like landmine, pipes, etc. Most GPR acquisition devices transmit a Ricker wavelet of small duration leading to a large bandwidth [1]. The penetration of the electromagnetic wave in the ground, and therefore the capability of detecting buried objects, will be linked to the frequency. In most applications, the GPR is composed of a monostatic antenna with a given sub-aperture, though more elaborate radar systems can be used. For instance, a stepped frequency signal is used in [3]. In this case, the data size is too large and a compressive sensing strategy has been developed to form the image. Another example is [4] where the authors propose a GPR based on a Multiple-Input Multiple-Output (MIMO) radar with multipolarisation. These new degrees of freedom allow to obtain a better resolution in the final image. In this paper, we will consider a monostatic Radar system which transmits a Ricker wavelet.

Several papers on buried objects detection using a GPR are devoted to landmine detection, which are objects located close to the ground. In this case, the response of the ground, called clutter, is very strong and leads to a high false alarm rate. A Kalman filter has been used in [5] to perform the detection/localisation. An improvement of this paper by using a particle filter is given in [6]. An approach based on a correlation method has been developed in [7] to remove the clutter. A method based on hidden Markov model has been recently proposed in [8]. All these methods have good performances because even if the Signal to Noise Ratio (SNR) is weak due to the clutter, the response of the landmine is also strong. In this case where the signal level is high enough, an inverse problem approach is a reliable method both to identify and reconstruct the target, as in [9, 10]. This is also the case when using GPR systems [11]. However in our case, the buried objects are located deeper in the subsoil and their response levels decrease quickly, shifting the problem towards a detection issue rather than identification. Thus, we have to find other strategies. In particular, we know that the response of the buried objects is close to an hyperbola due to the displacement of the radar. Using this information, some algorithms have been developed based on pattern recognition [12], Hough transform [13], etc. In particular, a standard method in GPR processing is to perform a coherent combination of radar traces, called *Migration* [1], in order to obtain a single target point for each buried object. This approach is also used in the Synthetic Aperture Radar (SAR) [14] config-

uration where the raw data is also composed of several hyperbola which are the responses of all scatterers located in the ground. But in SAR, the speed of the electromagnetic wave is known whereas in GPR applications, the wave speed is unknown and multiple layers could be present and be located between the ground and the buried objects. Several approaches are used to estimate the dielectric and the layer parameters of the subsoil, see for instance [15, 16]. In [17], the link between an estimation error on the dielectric constant and the depth localisation is shown. The problem of subsurface layers is also encountered in the domain of *Through-the-Wall* SAR [18] where the clutter can be removed for example by a subspace projection [19]. But this last method could be deficient in our case because this subspace operation removes a part of the hyperbola and then still reduces the response of the buried pipe. Therefore, the standard operation in GPR prospecting to detect pipes within layer interfaces is to perform a subspace projection by means of the Singular Value Decomposition (SVD), followed by the migration algorithm. However, the response of the objects remains weak and leads to poor detection. In addition, this method requires an estimate of the relative permittivity value ϵ'.

In this paper, we develop an algorithm in order to detect and to locate buried pipes located between 1 and 3 meters underground by taking into account the estimation of the dielectric constant. For this derivation, we are based on the radar detection/estimation framework initially given in [20]. The proposed detector depends on a signal of interest, this being the theoretical response of a buried pipe. This signal is concatenated in a vector denoted *steering vector* by analogy with existing work in the SAR domain [21], [22], [23]. This steering vector is built from the theoretical hyperbolas and the known transmitted signal. It is parametrised by the position in the ground and the local relative permittivity which are unknown. In practice, a noise corrupts the received signal. This noise is a combination of the electronic noise, clutter (the responses of the different subsurface layers) but also small buried objects such as rocks. If we consider that the noise is modelled by a Gaussian vector of zero mean and of an unknown covariance matrix, we can derive the corresponding adaptive detector from the Generalised Likelihood Ratio Test (GLRT) [24]. An easier approach is denoted by the "2-Step" GLRT [25]: the GLRT is first derived by assuming that the covariance matrix is known and its true value is replaced by its Maximum Likelihood Estimator (MLE), which is the so-called Sample Covariance Matrix (SCM) in the detector. Unfortunately, the Gaussian distribution seems to be inadequate in this configuration: the clutter or the presence of small objects, denoted in the following outliers, tends to create signals with strong heterogeneity. In this case, it is well known in sev-

eral applications, such as radar, finance, etc., that the Gaussian distribution is not adapted. A family of statistical distributions that is well adapted for this kind of modelling would be the Real Elliptic Symmetric (RES) distributions. Here, a a survey is available in [26] for the complex case. In this paper, we are interested in a sub-family of RES, the Spherical Invariant Random Vector (SIRV) [27] where the random vector is the product of a Gaussian vector and a positive number, called the texture. In this configuration, the derivation of the detector leads to the well-known Normalised Matched Filter (NMF) [28], [29]. In this detector, an estimate of the covariance matrix replaces the true covariance matrix to obtain the Adaptive NMF (ANMF). For this estimation, we can derive the MLE of the covariance matrix of a SIRV, denoted the Tyler's estimator [30], [31], [32], [33]. This estimator is well-known to be robust to strong heterogeneity and outliers. Nevertheless, a recent paper [34] shows that it could be suffering from bad estimation for some specific outliers. The authors recommend to use another estimate of the covariance matrix in the family of the M-estimators [35], [26]: the Huber's estimator [36], [37], [38] which is the combination of the SCM and the Tyler's estimator. In the paper, we will compare both the Tyler's and the Huber's estimators.

A major problem in adaptive detection comes from the estimation of the covariance matrix. This estimation needs a set of K *independent and identically distributed* (*i.i.d.*) data without the desired signal (here the response of a buried object), denoted secondary data. Moreover the number of data could be significant because a correct estimation needs $K = 2N$ where N is the data size [39]. In our configuration, the data size is really high (around 100) and it is impossible to have a set of secondary data. Several strategies exist to reduce the needed number of secondary data. For example, if the clutter is known to be low-rank and this rank is known, the covariance matrix can be replaced by an orthogonal projector [40], [41]. In most cases, the covariance matrix is known to have a particular structure which allows to reduce the number of variables we wish to estimate [42], [43], [44]. But the most common approach is to regularise the estimation: this introduces a bias, but lead in general to great performances even when only a small set of secondary data is available. The drawback is the choice of the regularisation parameter: for the SCM, Ledoit and Wolf [45] have proposed a strategy which is adapted to array processing in [46]. Several papers are devoted to the regularised version of the Tyler's estimator. The existence of the estimator as a function of the parameter of regularisation is proven in [47, 48]. An optimal parameter of regularisation is proposed in [49]. For the Huber's estimator, the existence has been proven in [49], but no criteria has been defined to estimate the optimal value.

One of the most important properties of those estimators is that they have a constant false alarm rate (CFAR) for a set threshold value, regardless of the noise power. Therefore, we propose in this paper to estimate the optimal regularisation parameter by choosing the value which ensures the most stable CFAR behaviour, by means of simulations. The corresponding detectors will be tested on simulated data and real data provided by the company ENGIE.

To summarise, this paper proposes the derivation of a robust adaptive detector where the dielectric constant has to be estimated and which needs a small set of secondary data in order to detect buried pipes, in the presence of subsurface layers and outliers. This detector allows to detect pipes with a low response level and to remove the subsoil layers and other noise contributions in the resulting image. It also provides a local estimation of the dielectric constant and finally keeps a CFAR behaviour regardless of the noise statistics.

This paper is organised as follows. Section 2 presents the signal model. The robust adaptive detector is derived in Section 3. In particular, we study the different regularised estimators by means of simulations. In Section 4, the proposed approach is tested on real data and compared to standard processing techniques. Section 5 draws some conclusions from this study.

The following convention is adopted: italic indicates a scalar quantity, lower case boldface indicates a vector quantity and upper case boldface a matrix. Notation ^{T} denotes the transposition operator. $E[\,]$ is the expected value operator. $\mathcal{N}(\mathbf{a}, \mathbf{M})$ is a real Gaussian vector with mean $\mathbf{a}$ and covariance matrix $\mathbf{M}$. The $N \times N$-identity matrix is denoted $\mathbf{I}_N$. $[\boldsymbol{A}]_{ij}$ is the element of matrix $\boldsymbol{A}$ at row i, column j.

2. Signal modelling

2.1. GPR Signal modelling

In the following, we consider a GPR moving along a u-axis, parallel to the ground (y-axis) and at a height h from it. At every position u_m, the radar emits a signal $e(t)$ in the ground. This signal is reflected by P scatterers in the ground, characterised by their reflection coefficients $a_p \in [-1\,;\,1]$, $p \in [\![1\,;\,P]\!]$ which represent the quantity of signal backscattered towards the radar. The echo of the signal on one scatterer p positioned at (y_p, z_p) and received by the radar is expressed as a time-delayed version of the emitted signal:

$$r_{m,p}(t) = a_p e\left(t - \tau_m(y_p, z_p)\right), \tag{1}$$

where τ_m is the time taken by the signal to travel from the radar to the scatterer and back. For a general configuration where the soil is composed of L layers, each of dielectric constant ϵ'_l, and the radar is not in a direct contact with the ground, $\tau_m(y,z)$ is [1]:

$$\tau_m(y,z) = \frac{2}{c_0}\left(d_{m,air}(y,z) + \sum_{l=1}^{L}\sqrt{\epsilon'_l}d_{m,l}(y,z)\right), \tag{2}$$

where $d_{m,l}$ and $d_{m,air}$ are respectively the distances travelled (single travel) by the wave through the layer l and the air.

The radar then receives the sum of all P echoes from the scatterers:

$$\begin{array}{rcl} r_m(t) & = & \sum_{p=1}^{P} r_{m,p}(t), \\ r_m(t) & = & \sum_{p=1}^{P} a_p e\left(t - \tau_m(y_p,z_p)\right). \end{array} \tag{3}$$

GPR systems usually return digital data to analyse, we thus consider that the imaged scene is divided in $N_y \times N_z$ pixels, each considered as a potential scatterer, and observe the received signals over N_T discrete time samples $t_i, i \in [\![1; N_T]\!]$. We create a vector $\boldsymbol{a} \in \mathbb{R}^{N_y N_z}$, $\boldsymbol{a} = [a_1 \dots a_p \dots a_{N_y N_z}]^T$, containing all the reflection coefficients arranged in lexicographic order, and build a set of matrices $\boldsymbol{H}_m \in \mathbb{R}^{N_T \times N_y N_z}$, with the element at line i and column p:

$$[\boldsymbol{H}_m]_{ip} = e(t_i - \tau_m(y_p,z_p)). \tag{4}$$

We then express the sampled version of the received signal $\boldsymbol{r}_m$ by the radar at position u_m:

$$\boldsymbol{r}_m = \boldsymbol{H}_m \boldsymbol{a}. \tag{5}$$

By concatenating all the $\boldsymbol{H}_m$ matrices into $\boldsymbol{H} \in \mathbb{R}^{N_T M \times N_y N_z}$,

$$\boldsymbol{H} = \left[\boldsymbol{H}_1^T \ \dots \ \boldsymbol{H}_M^T\right]^T,$$

and the vectors $\boldsymbol{r}_m$ into $\boldsymbol{r} \in \mathbb{R}^{N_T M}$, $\boldsymbol{r} = [\boldsymbol{r}_1 \ \dots \ \boldsymbol{r}_M]^T$, we get the full GPR scan image formation problem:

$$\boldsymbol{r} = \boldsymbol{H}\boldsymbol{a}. \tag{6}$$

This formulation of the problem opens prospects in terms of optimisation solutions, like minimising the cost function $\|\boldsymbol{r} - \boldsymbol{H}\boldsymbol{a}\|^2$. However, such inversion method is sensitive to noise and has a high computational cost. One can try to regularise the problem by invoking the inherent sparsity in the image (only

few pipes or scatterers buried) leading to ℓ_1 optimisation problems, minimising $\|\boldsymbol{r} - \boldsymbol{H}\boldsymbol{a}\|^2 + \lambda\|\boldsymbol{a}\|_1$ for instance. Such sparsity-driven techniques, among others, have been successfully used in SAR reconstruction [50], but some pipes response are too close to noise level and are blurred by the regularisation, rendering the process destructive. In addition, the apparent simplicity of the post-migration image geometry makes finding a suitable discriminating sparsity basis difficult. One can also resort to compressive sensing techniques as in [51, 3] when there is a high redundancy of information in the data, for instance when acquired with a stepped-frequency GPR. This redundancy is however not present in our case. Thus other approaches to the buried object detection problem are needed, and we propose a new method based on statistical tests for detection.

2.2. Detection problem

Because the GPR antenna emits signals with a wide beam pattern, buried objects in the ground can backscatter signals from different radar positions. As a consequence, hyperbolic shapes appear on the scan image. Thus, trying to detect a buried pipe at a particular position (y, z) in the ground is equivalent to checking the presence of a reflection hyperbola near the sampled position. To do that, we sample the pixels around the position (y, z) while following the shape of the hyperbola, determined by the delays of the backscattered signals received by the radar from the tested position, $\tau_m(y, z)$. This process is summarised in fig. 1. To reduce the complexity of the whole detection algorithm in terms of variables, we consider a simplified ground model in (2), where there is only one layer of dielectric constant ϵ', and the radar is in direct contact with the ground ($d_{air} = 0$). More complex models can be used in the computation of $\tau_m(y, z)$ if needed, without having to modify the sampling approach.

This sampling can be formalised in matrix form. From the signal $\boldsymbol{r}$, the signal $\boldsymbol{x}$ to be tested is extracted by means of a selection matrix $\boldsymbol{T}_{\epsilon',y,z} \in \{0; 1\}^{N \times MN_T}$, unique to each position (y, z). This matrix is built as follows: if the ith component of the tested vector $\boldsymbol{x}$ is set to be the jth component of $\boldsymbol{r}$ then $[\boldsymbol{T}_{\epsilon',y,z}]_{ij} = 1$, otherwise $[\boldsymbol{T}_{\epsilon',y,z}]_{ij} = 0$. We have:

$$\boldsymbol{x}_{\epsilon',y,z} = \boldsymbol{T}_{\epsilon',y,z}\boldsymbol{r}. \tag{7}$$

This signal $\boldsymbol{x}_{\epsilon',y,z}$ is then tested under two hypotheses: either it contains only noise $\boldsymbol{n}$, which characteristics are defined in the next subsection, or it is a set pattern $\boldsymbol{p}$, called steering vector, multiplied by a scaling factor $a_{\epsilon',y,z}$ and with added noise $\boldsymbol{n}$.

$$\begin{cases} H_0 \ : \ \boldsymbol{x}_{\epsilon',y,z} = \boldsymbol{n}, \\ H_1 \ : \ \boldsymbol{x}_{\epsilon',y,z} = a_{\epsilon',y,z}\boldsymbol{p} + \boldsymbol{n}. \end{cases} \tag{8}$$

In the following, to limit variable cluttering in the equations, we will denote $\boldsymbol{x} = \boldsymbol{x}_{\epsilon',y,z}$ and $a = a_{\epsilon',y,z}$.

The steering vector $\boldsymbol{p}$ is built as if being the vector $\boldsymbol{x}$ sampled from the ideal theoretical reflection hyperbola. To limit the size of the steering vector, we only sample the most representative points of the Ricker wavelet, being the extrema (the central and the two peripheral peak values), as shown in fig. 1.

Along the vector $\boldsymbol{x}$, we sample a set of secondary data $\{\boldsymbol{x}_k\}_{1,K}$ following the same procedure, for positions located at the same depth z than $\boldsymbol{x}$, while respecting a safe zone along the y-axis to prevent any signal being inadvertently sampled in this secondary set. It will be used in later sections to estimate the noise $\boldsymbol{n}$ characteristics.

2.3. Noise modelling

To derive the detector corresponding to the solution of problem (8), we have to propose a modelling for the noise $\boldsymbol{n}, \boldsymbol{n}_k \in \mathbb{R}^N$. In the paper, we will consider two cases: Gaussian and SIRV noise models to take into account to the heterogeneity of the data.

Gaussian modelling. In this case, the noise $\boldsymbol{n}$ follows a zero-mean Gaussian process $\mathcal{N}(\mathbf{0}, \mathbf{R})$ where $\mathbf{R}$ is the covariance matrix. We assume that this covariance matrix is unknown. We also assume that the secondary data $\{\boldsymbol{x}_k\}_{1,K}$ follow a zero-mean Gaussian process $\mathcal{N}(\mathbf{0}, \sigma\mathbf{R})$ where $\mathbf{R}$ is the same covariance matrix and σ is an unknown deterministic parameter. This last parameter allows to model a difference of power between the data under test and the secondary data. Nevertheless, this assumes that the power for all secondary data is the same, which is not realistic in many applications and in particular for GPR images. Therefore, we propose another modelling in the following paragraph.

SIRV modelling. We consider that the power can be different between data $\boldsymbol{x}_k$ and the data under test. In such a situation, it is common to model the corresponding clutter by a SIRV [52]. A SIRV is a non-homogeneous Gaussian random vector with random power. The SIRVs [27] $\boldsymbol{n}$, $\boldsymbol{n}_k$ are respectively the product of positive random variables τ, τ_k, called the texture, and N-dimensional vectors $\boldsymbol{g}$, $\boldsymbol{g}_k$ which follow independent Gaussian processes $\mathcal{N}(\mathbf{0}, \boldsymbol{R})$:

$$\begin{array}{rcl} \boldsymbol{n} & = & \sqrt{\tau}\boldsymbol{g}, \\ \boldsymbol{n}_k & = & \sqrt{\tau_k}\boldsymbol{g}_k. \end{array} \tag{9}$$

In the sequel, for identifiability issue, we consider $\mathrm{Tr}(\boldsymbol{R}) = N$.

3. Detection

To derive a detector solving the problem (8), we can resort to the GLRT framework. The goal is to maximise the following Likelihood Ratio Test (LRT) for the Gaussian case [20]:

$$\Lambda = \frac{\max\limits_{\sigma\in\mathbb{R}^+,\mathbf{R}\in\mathbb{R}^{N\times N}\ a\in\mathbb{R},\epsilon'\in\mathbb{R}^+} L(\boldsymbol{x}|H_1)}{\max\limits_{\sigma\in\mathbb{R}^+,\mathbf{R}\in\mathbb{R}^{N\times N}} L(\boldsymbol{x}|H_0)} \tag{10}$$

where $L(\boldsymbol{x}|H_i)$ is the density of probability of the data $\boldsymbol{x}$ under H_0 or H_1. For the SIRV case, we consider that the textures are unknown deterministic variables and therefore, the LRT is written as follows:

$$\Lambda = \frac{\max\limits_{\tau,\tau_k\in\mathbb{R}^+,\mathbf{R}\in\mathbb{R}^{N\times N}\ a\in\mathbb{R},\epsilon'\in\mathbb{R}^+} L(\boldsymbol{x}|H_1)}{\max\limits_{\tau,\tau_k\in\mathbb{R}^+,\mathbf{R}\in\mathbb{R}^{N\times N}} L(\boldsymbol{x}|H_0)}. \tag{11}$$

Therefore, two solutions exist for the detection. The first one is to solve the previous LRT by integrating the secondary data $\{\boldsymbol{x}\}_k$ and to resort the GLRT as in [24]. But this solution is quite difficult to apply to the SIRV case, so the common procedure is first to derive the detector by assuming that the covariance matrix $\mathbf{R}$ is known, and then replace it by an appropriate estimator of the covariance matrix. In [25], the performances of the two approaches are shown to be close for a Gaussian modelling.

3.1. Derivation of the detector with known $\boldsymbol{R}$

When the covariance matrix is assumed to be known, the derivation of both LRT (10) and (11) leads to the same detector [29], [53], [28] which is here parametrised by the dielectric constant ϵ':

$$\Lambda = \max_{\epsilon'\in\mathbb{R}^+} \frac{|\boldsymbol{p}^T\boldsymbol{R}^{-1}\boldsymbol{x}|^2}{(\boldsymbol{p}^T\boldsymbol{R}^{-1}\boldsymbol{p})(\boldsymbol{x}^T\boldsymbol{R}^{-1}\boldsymbol{x})}. \tag{12}$$

We recall that the parameter ϵ' governs the transformation $\boldsymbol{T}_{\epsilon',y,z}$ which allows to build the data vector $\boldsymbol{x}$ from the raw data $\boldsymbol{r}$. Finally the detector is compared to a threshold to decide either hypothesis H_1 or H_0:

$$\Lambda \underset{H_1}{\overset{H_0}{\lessgtr}} \eta. \tag{13}$$

The decision threshold η is often set by fixing a Probability of False Alarm (PFA). For this setting, it is usual if possible to compute the distribution of the detector which allows to have the theoretical relation PFA as a function of the threshold. For the NMF of Eq. (12), the relation is known [29]:

$$\eta = 1 - \text{PFA}^{\frac{1}{N-1}}. \tag{14}$$

When the distribution is not available, we have to estimate the relation threshold-PFA by means of Monte Carlo trials.

3.2. Plug-in of the covariance matrix estimator

In this section, we present different estimators of the covariance matrix. The problem addressed in this paper is that the number of secondary data available K can be inferior to the data size N, leading the inversion in Eq. (12) to be inconsistent. Therefore, it is necessary to develop a strategy for efficient estimation in presence of a small number of secondary data. Since, we do not assume any structure (low-rank, Toeplitz) for the covariance matrix, we propose to use shrinkage estimators of the covariance matrix which have deserved great interest these last years in the signal processing community. First, we consider the Gaussian case in the following section.

3.2.1. Gaussian case

In this case, the most effective method is to replace the true covariance matrix by its Maximum Likelihood Estimators (MLE), the Sample Covariance Matrix (SCM):

$$\hat{\boldsymbol{R}} = \frac{1}{K}\sum_{k=1}^{K} \boldsymbol{x}_k \boldsymbol{x}_k^T. \tag{15}$$

In the under-sampled case, the seminal paper [45] proposes the following estimator:

$$\tilde{\boldsymbol{R}} = \beta\hat{\boldsymbol{R}} + \alpha\boldsymbol{I}, \tag{16}$$

where β and α have to be estimated. In this paper, the estimation of the shrinkage parameters is performed by minimising the following MSE [46]:

$$\text{MSE}(\tilde{\boldsymbol{R}}) = E[\|\tilde{\boldsymbol{R}} - \boldsymbol{R}\|^2]. \tag{17}$$

In this case, we have:

$$\begin{array}{rcl} \hat{\alpha} & = & \min\left[\hat{\nu}\frac{\hat{\rho}}{\|\hat{\boldsymbol{R}}-\hat{\nu}\boldsymbol{I}\|^2}, \hat{\nu}\right] \\ \hat{\beta} & = & 1 - \frac{\hat{\alpha}}{\hat{\nu}}, \end{array}, \tag{18}$$

where

$$\begin{array}{rcl} \hat{\rho} & = & \frac{1}{K^2}\sum_{k=1}^{K}\|\boldsymbol{x}_k\|^4 - \frac{1}{K}\|\hat{\boldsymbol{R}}\|^2, \\ \hat{\nu} & = & \frac{\text{tr}(\hat{\boldsymbol{R}})}{N}. \end{array} \tag{19}$$

3.2.2. SIRV case

In the over-sampled configuration (when $K > N$), the MLE of the covariance matrix is called the Tyler's estimator (or Fixed Point Estimator) and is:

$$\hat{\boldsymbol{R}} = \frac{N}{K}\sum_{k=1}^{K}\frac{\boldsymbol{x}_k\boldsymbol{x}_k^T}{\boldsymbol{x}_k^T\hat{\boldsymbol{R}}^{-1}\boldsymbol{x}_k}. \tag{20}$$

Since the matrix depends on an implicit function, we have to resort an iterative algorithm to compute the solution:

$$\hat{\boldsymbol{R}}_{k+1} = \frac{N}{K}\sum_{k=1}^{K}\frac{\boldsymbol{x}_k\boldsymbol{x}_k^T}{\boldsymbol{x}_k^T\hat{\boldsymbol{R}}_k^{-1}\boldsymbol{x}_k}. \tag{21}$$

This algorithm is known to converge towards to the correct solution [54].

Nevertheless, this estimator is inconsistent in under-sampled configuration when $K < M$. In this case, we can add an additional diagonal loading as initially proposed in [55]. Therefore, the convergence is not ensured and a choice of the parameter of the diagonal loading has to be considered. In [48], [56], it has been proven that the following equation:

$$\hat{\boldsymbol{R}} = (1-\alpha)\frac{N}{K}\sum_{k=1}^{K}\frac{\boldsymbol{x}_k\boldsymbol{x}_k^T}{\boldsymbol{x}_k^T\hat{\boldsymbol{R}}^{-1}\boldsymbol{x}_k} + \alpha\boldsymbol{I} \tag{22}$$

admits an unique solution for $\alpha \in [max(0, 1-\frac{K}{N}), 1]$. The following algorithm allows to reach this solution:

$$\hat{\boldsymbol{R}}_{k+1} = (1-\alpha)\frac{N}{K}\sum_{k=1}^{K}\frac{\boldsymbol{x}_k\boldsymbol{x}_k^T}{\boldsymbol{x}_k^T\hat{\boldsymbol{R}}_k^{-1}\boldsymbol{x}_k} + \alpha\boldsymbol{I}. \tag{23}$$

This last result involves a parameter selection which ensures the convergence, but with no guarantee of optimality. In [49], by minimising the following MSE:

$$\text{MSE} = E[\|\boldsymbol{R}^{-1}\boldsymbol{R}_\alpha - \frac{1}{N}\,\text{Tr}(\boldsymbol{R}^{-1}\boldsymbol{R}_\alpha)\boldsymbol{I}\|^2] \tag{24}$$

where $\boldsymbol{R}_\alpha$ is a *clairvoyant estimator* of $\boldsymbol{R}$:

$$\boldsymbol{R}_\alpha = (1-\alpha)\frac{N}{K}\sum_{k=1}^{K}\frac{\boldsymbol{x}_k\boldsymbol{x}_k^T}{\boldsymbol{x}_k^T\boldsymbol{R}^{-1}\boldsymbol{x}_k} + \alpha\boldsymbol{I}, \tag{25}$$

we can obtain an estimator:

$$\hat{\alpha} = \frac{N\,\mathrm{Tr}(\hat{\boldsymbol{R}}) - 1}{N\,\mathrm{Tr}(\hat{\boldsymbol{R}}) - 1 + K(N+1)(N^{-1}\,\mathrm{Tr}(\hat{\boldsymbol{R}}^{-2}) - 1)} \tag{26}$$

where $\hat{\boldsymbol{R}}$ is any solution of (23) with $\alpha \in [max(0, 1-\frac{K}{N}), 1]$.

The Tyler's estimator is known to be robust to the statistic of the noise and the presence in the secondary data of outliers. Nevertheless, in a recent paper [34], the authors proved that the Tyler's estimator is sensitive to data contamination for some specific configurations. In this case, it could be preferable to use the M-estimators of the covariance matrix which are defined by the following implicit function:

$$\hat{\boldsymbol{R}} = \frac{1}{K}\sum_{k=1}^{K}\psi\left(\boldsymbol{x}_k^T\hat{\boldsymbol{R}}^{-1}\boldsymbol{x}_k\right)\boldsymbol{x}_k\boldsymbol{x}_k^T \tag{27}$$

where ψ depends on the pdf of the texture. In practice as in this paper, its pdf is assumed to be unknown. In that case, one can resort to M-estimators [35], [36], [26] and use a new functional that is not related to the texture pdf. For example, we have the Huber's estimator:

$$\hat{\boldsymbol{R}} = \frac{1}{K}\sum_{k=1}^{K}u\left(\boldsymbol{x}_k^T\hat{\boldsymbol{R}}^{-1}\boldsymbol{x}_k\right)\boldsymbol{x}_k\boldsymbol{x}_k^T \tag{28}$$

where

$$u(t) = \begin{cases} 1, & \text{for } t \leq c^2 \\ c^2/t, & \text{for } t > c^2 \end{cases} \tag{29}$$

with $c > 0$.

As for the Tyler's estimator, we can build an under-sampled version of this estimator [49]:

$$\hat{\boldsymbol{R}} = \frac{1}{K}\sum_{k=1}^{K}u\left(\boldsymbol{x}_k^T\hat{\boldsymbol{R}}^{-1}\boldsymbol{x}_k\right)\boldsymbol{x}_k\boldsymbol{x}_k^T + \alpha\boldsymbol{I}. \tag{30}$$

The following iterations

$$\hat{\boldsymbol{R}}_{k+1} = \frac{1}{K}\sum_{k=1}^{K}u\left(\boldsymbol{x}_k^T\hat{\boldsymbol{R}}_k^{-1}\boldsymbol{x}_k\right)\boldsymbol{x}_k\boldsymbol{x}_k^T + \alpha\boldsymbol{I} \tag{31}$$

allow to reach an unique solution for any α and for any initial value $\hat{\boldsymbol{R}}_0$ [49]. For the best of our knowledge, the literature has not provide a method for computing optimal value α. In the following, we propose to estimate an optimal value by minimising the PFA or maximising the PD.

3.2.3. Adaptive detectors

When an estimation of the covariance matrix is computed, it can be plugged into the NMF detector (12) which leads to an Adaptive NMF (ANMF), denoted $\hat{\Lambda}$. As said before, it is interesting to derive the distribution of the detector in order to set the threshold for a given PFA. For the SCM, this distribution has been derived in [57] for the Gaussian case and an approximate distribution has been proposed in [38] for CES case. Unfortunately, such a distribution is really difficult to compute when shrinkage estimators of the covariance matrix are used in the ANMF.

Therefore, we propose in the following subsection to estimate the relation PFA-threshold by means of Monte Carlo trials for all ANMF built from a shrinkage estimator of the covariance matrix (SCM, Tyler and Huber). We will also compute the PD as a function of the SNR. Moreover, we will estimate the parameter of the shrinkage for the Huber's estimator by choosing the value that ensures a CFAR behaviour regardless of noise heterogeneity.

3.3. Simulation

We consider the three adaptive detectors: $\hat{\Lambda}_{SCM}$, $\hat{\Lambda}_{Tyler}$ and $\hat{\Lambda}_{Huber}$ built by replacing in the NMF of Eq. (12) the true covariance matrix by the regularised versions of the SCM (16), the Tyler's estimator (22) and the Huber's estimator (30), along with the limit cases $\hat{\Lambda}_{White}$ and $\hat{\Lambda}_{Oracle}$. These limit cases are such that $\hat{\boldsymbol{R}} = \boldsymbol{I}_N$ for the white noise hypothesis and, for Oracle case, $\boldsymbol{R}$ is the real covariance matrix of the generated noise. The simulation consists in successive Monte-Carlo trials, in order to estimate the PFA as a function of the threshold and the PD as a function of the SNR for the various estimators.

The simulation is set up with a SIRV noise, the Gaussian vector having a widely-used covariance matrix model of Toeplitz form $[\boldsymbol{R}]_{ij} = \rho^{|i-j|}$, where we have considered $\rho = 0.9$. The texture factor generated follows a gamma law $\Gamma(\nu, \frac{1}{\nu})$: parameter $\nu = 2$ leads to a near-Gaussian noise whereas parameter $\nu = 0.1$ yields a more impulsive noise. The steering vector has size $N = 153$ corresponding to the sampling of 3 signal points on 51 columns of a GPR image, 25 on each side of the tested position. The number considered for secondary data is $K = 40$. Both PFA and PD values were estimated by averaging over

100000 MC trials. PD values are given for fixed threshold values corresponding to PFA $= 10^{-2}$ for each estimator. For each SNR value, the corresponding scaling factor a from Eq. (8) has been computed as:

$$a = \sqrt{\text{SNR Tr}(\boldsymbol{R})}, \tag{32}$$

this value being valid only if the steering vector $\boldsymbol{p}$ has been normalised, $\|\boldsymbol{p}\| = 1$.

Fig. 2 shows the PFA-Threshold and PD-SNR graphs for Huber's estimator when the regularisation parameter $\alpha = 0.05, 0.1, 0.25, 0.5, 0.75, 0.9$. The graphs show that in the near-Gaussian case, there is little variability in terms of probability of detection, but a strong regularisation parameter value gives a slightly better PFA, for a fixed threshold value. The same observation holds true for the impulsive noise case: there is still little variability in the probability of detection for several α values, but this time, the PFA versus threshold curves are reversed. Low α values give stable PFA-Threshold values in both near-Gaussian and impulsive noise cases, appearing as a good choice for cases where the noise model is not known.

Fig. 3 shows the PFA-Threshold and PD-SNR graphs for all estimators respectively for $\nu = 2$ and $\nu = 0.1$. The SCM estimator is given with the regularisation parameters computed as in Eq. (18), Huber's estimator is given with $\alpha = 0.75$, and Tyler's estimator is computed with $\alpha = 1 - 0.9\frac{K}{N}$ and α_0 of Eq. (26) (we set $\beta = 1-\alpha$). The regularised estimators show good results. Though Tyler's estimator with $\beta = 0.9\frac{K}{N}$ has a higher PFA in near Gaussian noise, it still gives the best probability of detection, greatly outperforming the others for the more impulsive SIRV noise. On the other hand, Tyler's estimator regularised with the optimal $\hat{\alpha}_0$ of Eq. (26), appearing as "Tyler opt" on the graphs, yields results close to the white noise limit case. This is explained by that $\hat{\alpha}_0$ is close to 1 in our case, leading to an estimated covariance matrix $\hat{\boldsymbol{R}}$ that is close to the identity matrix $\boldsymbol{I}_N$. On the contrary, the SCM estimator with optimal parameter values performs really well in the near-Gaussian case, and still give acceptable results in the impulsive noise case.

4. Numerical simulations on real data

In this section, we apply the three regularised detectors and the white noise limit case to real world data. We also compare them with standard GPR image processing migration method, with and without SVD preprocessing. The migration is performed using the Backprojection algorithm (BP) [14], $\epsilon' = 5$, and the

SVD preprocessing removes the first 4 singular values in the images. For all other estimators, parameters are kept identical to the previous statistical simulations, $N = 153$, $K = 40$. The SCM is computed with regularisation parameters from Eq. (18), Huber's estimator is computed with $\alpha = 0.25$, and Tyler's for $\beta = 0.9\frac{K}{N}$. The white noise case will help in showing the relevancy of the covariance matrix estimation.

Two GPR radargrams are used, acquired over a test site containing pipes of various size and materials buried in sand. Image *0039.RAD* (fig. 4a) has 156 radar positions. Image *0028.RAD* (fig. 4b) has 225 radar positions. The radar sampling step is 2.5 cm, both images have 512 time samples per position with a sampling frequency of 20 GHz and an emitted Ricker wavelet signal having peak frequency at 500 MHz. The first image contains two pipes, the second has five, and both images also contain a layer interface reflection visible between 5 and 10 ns on fig. 4 which is due to soil compaction. Pipes position and characteristics are given in table 1.

On figs. 5 and 6, the raw migrated image shows the necessity of a preprocessing in order to remove the layer which would, otherwise, raise the false alarm rate. While the SVD preprocessing improves the resulting migrated image, all ANMFs succeed better in removing the layer, with a lower residual level. This also proves the relevancy of the covariance matrix estimation as opposed to the white noise case. Huber's estimator shows some difficulties in the lower part of images. This may be due to zero-paddings performed to handle non-existent samples, and those null samples would lead the "normal" secondary data to be considered as outliers by the estimator. Finally, the ANMF with SCM and Tyler's estimators return similar results, sign that the data here is closer to Gaussian and without outliers, but also that there is no loss of performance in considering a more complex noise model.

Figs. 7 and 8 show the detection results for the migrated images and ANMFs. The threshold value is computed as a percentage of the maximum value of the image $Thres = \eta \max(\text{IM})$. In fig. 7, we used a threshold of $\eta = 0.5$, corresponding to the limit of detection of all pipes by at least one method. We used in fig. 8, a value of $\eta = 0.37$ corresponding to the limit of detection of four pipes (pushing the detection to 5 pipes would require a very small threshold value, leading a too high PFA for all detection results). Results show that the ANMFs have a slightly higher false alarm rate but give better results in terms of detection with four pipes detected in fig. 8d out of five, and two out of two in fig. 7d while the migration methods detect only two in fig. 8a and three pipes in fig. 8b, and one in figs. 7a, 7b. To further confront the methods, one could choose a threshold ensuring the same

detection rate for all estimators and migrations and then compare the PFA levels.

One observation on the results is the dual detection responses for certain pipes, whatever the method (see figs. 7 and 8). This is not yet fully explained at this time, but it can be due to that the corresponding pipe responses involve one Ricker wavelet followed by another but reversed and shifted "shadowed" Ricker wavelet. One should also note that this experiment was conducted for a single available ground fill type, though the CFAR behaviour of the detectors should ensure consistent results for other heterogeneous/textured ground compositions that follow SIRV property.

5. Conclusion

In this paper, we developed a robust adaptive method in order to detect and localise buried pipes situated under several subsurface layers. This detector is based on the ANMF and the estimation of the dielectric constant of the subsoil. In the derivation, the SIRV noise model was chosen in order to take into account data heterogeneity and the eventual presence of outliers (due to thermal noise, clutter from the subsurface layers and small rocks) in the data. Moreover, since the sample support for the estimation of the covariance matrix is small, we proposed to use regularised versions of the M-estimators. In simulated data, we evaluate the relation PFA-threshold for different ANMF detectors. In particular, we investigated the impact of the regularisation parameters on both PFA and PD. Application on real data and performance comparison with standard migration processes showed the interest of the approach in particular to detect buried pipes having very weak responses.

Future work will deal with a more elaborate modelling of the response of the buried pipe. For example, the width and/or the type of pipe could be integrated into the steering vector by using the subspace approaches of [21], [22] and [23].

Acknowledgment

We thank the ENGIE Company for providing GPR datasets and BPI France for funding this work. Also, we are grateful Sophie Reed for correcting English mistakes in this paper.

References

[1] D. J. Daniels, Ground Penetrating Radar, IEE, 2004.

[2] H. M. Jol (Ed.), Ground Penetrating Radar: Theory and Applications, Elsevier, 2009.

[3] A. Gurbuz, J. McClellan, W. Scott, A compressive sensing data acquisition and imaging method for stepped frequency GPRs, Signal Processing, IEEE Transactions on 57 (7) (2009) 2640–2650. doi:10.1109/TSP.2009.2016270.

[4] Z. Zeng, J. Li, L. Huang, X. Feng, F. Liu, Improving target detection accuracy based on multipolarization MIMO GPR, Geoscience and Remote Sensing, IEEE Transactions on 53 (1) (2015) 15–24. doi:10.1109/TGRS.2014.2312937.

[5] A. Zoubir, I. Chant, C. Brown, B. Barkat, C. Abeynayake, Signal processing techniques for landmine detection using impulse ground penetrating radar, Sensors Journal, IEEE 2 (1) (2002) 41–51. doi:10.1109/7361.987060.

[6] W. Ng, T. Chan, H. So, K. Ho, Particle filtering based approach for landmine detection using Ground Penetrating Radar, Geoscience and Remote Sensing, IEEE Transactions on 46 (11) (2008) 3739–3755.

[7] V. Kovalenko, A. Yarovoy, L. Ligthart, A novel clutter suppression algorithm for landmine detection with GPR, Geoscience and Remote Sensing, IEEE Transactions on 45 (11) (2007) 3740–3751. doi:10.1109/TGRS.2007.903694.

[8] A. Manandhar, P. Torrione, L. Collins, K. Morton, Multiple-instance hidden markov model for gpr-based landmine detection, Geoscience and Remote Sensing, IEEE Transactions on 53 (4) (2015) 1737–1745. doi:10.1109/TGRS.2014.2346954.

[9] M. Salucci, G. Oliveri, A. Randazzo, M. Pastorino, A. Massa, Electromagnetic subsurface prospecting by a multifocusing inexact newton method within the second-order born approximation, JOSA A 31 (6) (2014) 1167–1179.

[10] M. Salucci, G. Oliveri, A. Randazzo, M. Pastorino, A. Massa, Electromagnetic subsurface prospecting by a fully nonlinear multifocusing inexact newton method, JOSA A 31 (12) (2014) 2618–2629.

[11] M. Salucci, G. Oliveri, A. Massa, Gpr prospecting through an inverse-scattering frequency-hopping multifocusing approach, Geoscience and Remote Sensing, IEEE Transactions on 53 (12) (2015) 6573–6592.

[12] C. Maas, J. Schmalzl, Using pattern recognition to automatically localize reflection hyperbolas in data from ground penetrating radar, Computers and Geosciences 58 (2013) 116 – 125. doi:http://dx.doi.org/10.1016/j.cageo.2013.04.012.

[13] A. Simi, S. Bracciali, G. Manacorda, Hough transform based automatic pipe detection for array gpr: algorithm development and on-site tests, in: Radar Conference, 2008. RADAR'08. IEEE, IEEE, 2008, pp. 1–6.

[14] M. Soumekh, Synthetic aperture radar signal processing, Wiley - Interscience Publication, 1999.

[15] C. ping Kao, J. Li, Y. Wang, H. Xing, C. Liu, Measurement of layer thickness and permittivity using a new multilayer model from gpr data, Geoscience and Remote Sensing, IEEE Transactions on 45 (8) (2007) 2463–2470. doi:10.1109/TGRS.2007.900980.

[16] Z. lai Huang, J. Zhang, Determination of parameters of subsurface layers using gpr spectral inversion method, Geoscience and Remote Sensing, IEEE Transactions on 52 (12) (2014) 7527–7533. doi:10.1109/TGRS.2014.2313603.

[17] R. Wu, K. Gu, J. Li, M. Bradley, J. Habersat, G. Maksymonko, Propagation velocity uncertainty on gpr sar processing, Aerospace and Electronic Systems, IEEE Transactions on 39 (3) (2003) 849–861.

[18] M. G. Amin, F. Ahmad, Through-the-Wall Radar Imaging: Theory and Applications, E-reference Signal Processing, Elsevier, 2013.

[19] F. Tivive, A. Bouzerdoum, M. Amin, A subspace projection approach for wall clutter mitigation in Through-the-Wall Radar imaging, Geoscience and Remote Sensing, IEEE Transactions on 53 (4) (2015) 2108–2122. doi:10.1109/TGRS.2014.2355211.

[20] H. V. Trees, Estimation and modulation theory, Vol. 1, John Wiley and Sons, 2001.

[21] R. Durand, G. Ginolhac, L. Thirion, P. Forster, New SAR processor based on matched subspace detector, Aerospace and Electronic Systems, IEEE Transactions on 45 (1) (2009) 221–236.

[22] F. Brigui, G. Ginolhac, L. Thirion-Lefevre, P. Forster, New SAR target imaging algorithm based on oblique projection for clutter reduction, Aerospace and Electronic Systems, IEEE Transactions on 50 (2) (2014) 1118–1137.

[23] F. Brigui, L. Thirion-Lefevre, G. Ginolhac, P. Forster, New SAR algorithm based on orthogonal projections for MMT detection and interference reduction, Geoscience and Remote Sensing, IEEE Transactions on 52 (7) (2014) 3800–3811. doi:10.1109/TGRS.2013.2276417.

[24] E. Kelly, An adaptive detection algorithm, Aerospace and Electronic Systems, IEEE Transactions on 22 (1) (1986) 115–127.

[25] F. Robey, D. Fuhrmann, E. Kelly, R. Nitzberg, A CFAR adaptive matched filter detector, Aerospace and Electronic Systems, IEEE Transactions on 28 (2) (1992) 208 – 216.

[26] E. Ollila, D. Tyler, V. Koivunen, H. Poor, Complex elliptically symmetric distributions: Survey, new results and applications, Signal Processing, IEEE Transactions on 60 (11) (2012) 5597?5625.

[27] K. Yao, A representation theorem and its applications to spherically invariant random processes, Information Theory, IEEE Transactions on 19 (5) (1973) 600 – 608.

[28] E. Conte, M. Lops, G. Ricci, Adaptive matched filter detection in spherically invariant noise, IEE Signal Processing Letters (8).

[29] L. Scharf, B. Friedlander, Matched subspace detectors, Signal Processing, IEEE Transactions on 42 (8) (1994) 2146–2157.

[30] D. Tyler, Robustness and efficiency properties of scatter matrices, Biometrika 70 (2) (1983) 411.

[31] D. Tyler, A distribution-free m-estimator of multivariate scatter, Ann. Statist. 15 (1) (1987) 234?251.

[32] F. Gini, M. Greco, Texture modelling, estimation and validation using measured sea clutter data, IEE Proc. Radar, Sonar Navig. 149 (3) (2002) 115 – 124.

[33] F. Pascal, Y. Chitour, J. Ovarlez, P. Forster, P. Larzabal, Existence and characterization of the covariance matrix maximum likelihood estimate in spherically invariant random processes, Signal Processing, IEEE Transactions on 56 (1) (2008) 34 – 48.

[34] D. Morales-Jimenez, R. Couillet, M. McKay, Large dimensional analysis of robust m-estimators of covariance with outliers, Signal Processing, IEEE Transactions on 63 (21) (2015) 5784–5797. doi:10.1109/TSP.2015.2460225.

[35] R. Maronna, R. Martin, V. Yohai, Robust Statistics: Theory and Methods, Wiley Series in Probability and Statistics, 2006.

[36] P. Huber, Robust estimation of a location parameter, Ann. Math. Statist. 35 (1) (1964) 73 – 101.

[37] P. Huber, E. Ronchetti, Robust Statistics, Wiley, 2009.

[38] M. Mahot, F. Pascal, P. Forster, J. Ovarlez, Asymptotic properties of robust complex covariance matrix estimates, Signal Processing, IEEE Transactions on 61 (13) (2013) 3348–3356. doi:10.1109/TSP.2013.2259823.

[39] I. Reed, J. Mallett, L. Brennan, Rapid convergence rate in adaptive arrays, Aerospace and Electronic Systems, IEEE Transactions on AES-10 (6) (1974) 853 – 863.

[40] M. Rangaswamy, F. Lin, K. Gerlach, Robust adaptive signal processing methods for heterogeneous radar clutter scenarios, Signal Processing 84 (2004) 1653 – 1665.

[41] A. Breloy, G. Ginolhac, F. Pascal, P. Forster, Clutter subspace estimation in low rank heterogeneous noise context, Signal Processing, IEEE Transactions on 63 (9) (2015) 2173 – 2182.

[42] P. Forster, Generalized cross spectral matrices for array of arbitrary geometry, Signal Processing, IEEE Transactions on 49 (5) (2001) 972–978.

[43] I. Soloveychik, A. Wiesel, Tyler's covariance matrix estimator in elliptical models with convex structure, Signal Processing, IEEE Transactions on 62 (20) (2014) 5251 – 5259.

[44] Y. Sun, P. Babu, D. Palomar, Regularized robust estimation of mean and covariance matrix under heavy-tailed distributions, Signal Processing, IEEE Transactions on 63 (12) (2015) 3096–3109. doi:10.1109/TSP.2015.2417513.

[45] O. Ledoit, M. Wolf, A well-conditioned estimator for large-dimensional covariance matrices, Journal of multivariate analysis 88 (2004) 365–411.

[46] L. Du, J. Li, P. Stoica, Fully automatic computation of diagonal loading levels for robust adaptive beamforming, Aerospace and Electronic Systems, IEEE Transactions on 46 (1) (2010) 449–458. doi:10.1109/TAES.2010.5417174.

[47] Y. Chen, A. Wiesel, A. Hero, Robust shrinkage estimation of high-dimensional covariance matrices, Signal Processing, IEEE Transactions on 59 (9) (2011) 4097–4107. doi:10.1109/TSP.2011.2138698.

[48] F. Pascal, Y. Chitour, Y. Quek, Generalized robust shrinkage estimator and its application to stap detection problem, Signal Processing, IEEE Transactions on 62 (21) (2014) 5640–5651. doi:10.1109/TSP.2014.2355779.

[49] E. Ollila, D. Tyler, Regularized m -estimators of scatter matrix, Signal Processing, IEEE Transactions on 62 (22) (2014) 6059–6070. doi:10.1109/TSP.2014.2360826.

[50] M. Cetin, I. Stojanovic, N. O. Onhon, K. R. Varshney, S. Samadi, W. C. Karl, A. S. Willsky, Sparsity-driven synthetic aperture radar imaging: Reconstruction, autofocusing, moving targets, and compressed sensing, Signal Processing Magazine, IEEE 31 (4) (2014) 27–40.

[51] A. Massa, P. Rocca, G. Oliveri, Compressive sensing in electromagnetics-a review, Antennas and Propagation Magazine, IEEE 57 (1) (2015) 224–238.

[52] M. Rangaswamy, D. Weiner, A. Ozturk, Non-gaussian vector identification using spherically invariant random processes, Aerospace and Electronic Systems, IEEE Transactions on 29 (1) (1993) 111–124.

[53] E. Jay, J. Ovarlez, D. Leclercq, P. Duvaut, BORD: Bayesian optimum radar detector, Signal Processing 83 (6) (2003) 1151 – 1162.

[54] F. Pascal, P. Forster, J. Ovarlez, P. Larzabal, Performance analysis of covariance matrix estimates in impulsive noise, Signal Processing, IEEE Transactions on 56 (6) (2008) 2206 – 2217.

[55] Y. Abramovich, N. Spencer, Diagonally loaded normalised sample matrix inversion (lnsmi) for outlier-resistant adaptive filtering, in: Acoustics, Speech and Signal Processing, 2007. ICASSP 2007. IEEE International Conference on, Vol. 3, 2007, pp. III–1105–III–1108. doi:10.1109/ICASSP.2007.366877.

[56] W. Sun, H. So, F. Chan, L. Huang, Tensor approach for eigenvector-based multi-dimensional harmonic retrieval, Signal Processing, IEEE Transactions on 61 (13) (2013) 3378–3388.

[57] S. Kraut, L. Scharf, L. McWhorter, Adaptive subspace detectors, Signal Processing, IEEE Transactions on 49 (1) (2001) 1–16.

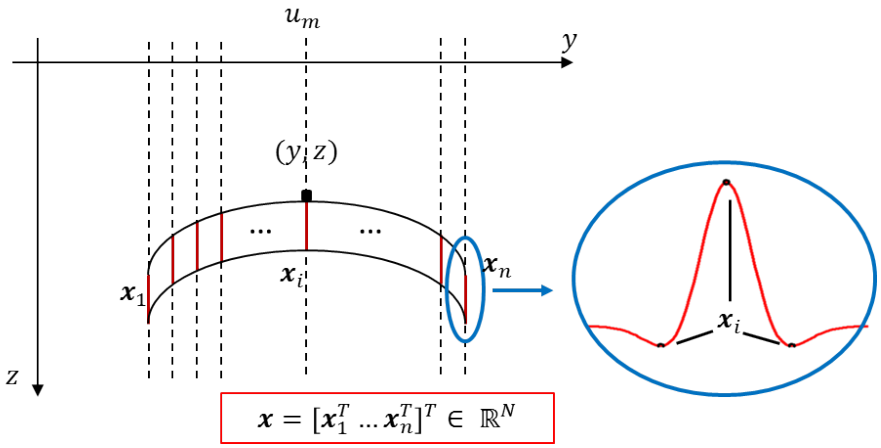

Figure 1: Sampling process for the vector $\boldsymbol{x}$: red lines represent the samples along the different columns of the image, which are then assembled in the vector $\boldsymbol{x}$. Only three values are sampled per column to limit the size of the data vector, the latter being the central and two peripheral peak values.

Table 1: Pipe characteristics in both datasets.

Dataset	0039.RAD		0028.RAD				
Material	PE	Steel	PE	PE	PE	Cast iron	Steel
Diameter (mm)	110	20	160	20	63	118	160
Position (m)	(2;0.84)	(3;0.84)	(1;1)	(2;1)	(3;1)	(4;1)	(5;1)

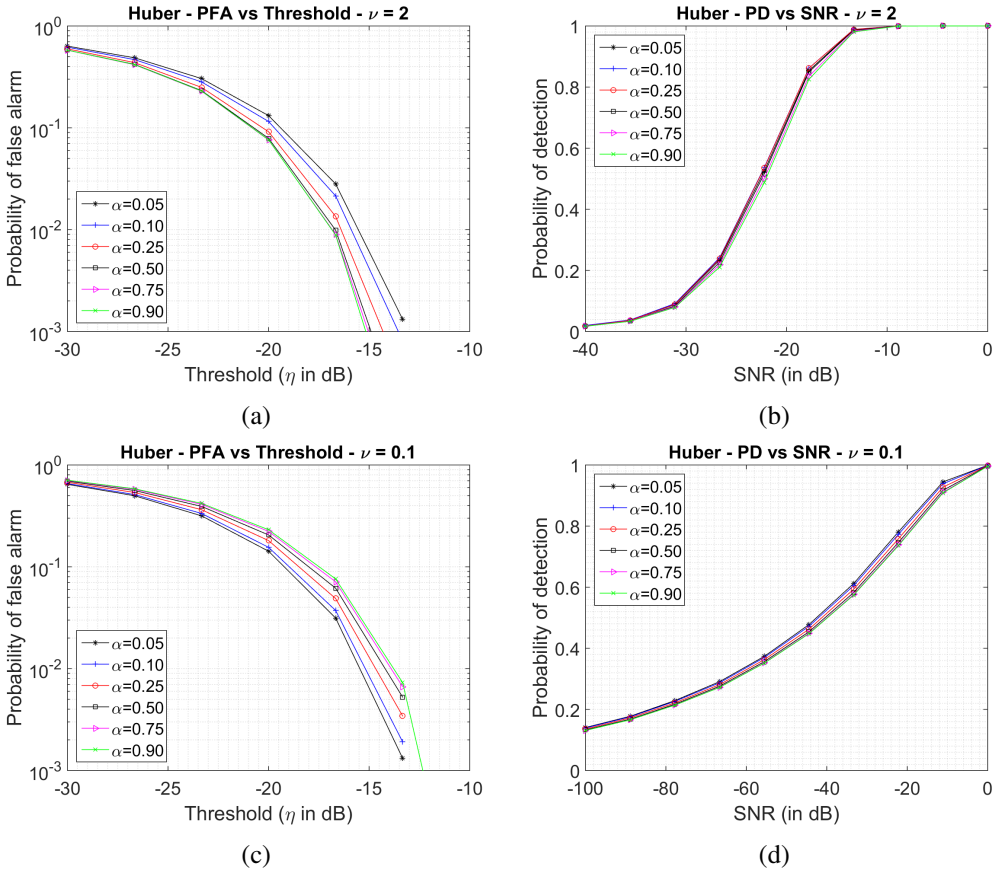

Figure 2: Huber's estimator performance curves for different values of α. (a) PFA versus Threshold ($\nu = 2$), (b) PD versus SNR ($\nu = 2$), (c) PFA versus Threshold ($\nu = 0.1$), (d) PD versus SNR ($\nu = 0.1$). $N = 153$, $K = 40$, $\alpha = 0.05, 0.1, 0.25, 0.5, 0.75, 0.9$.

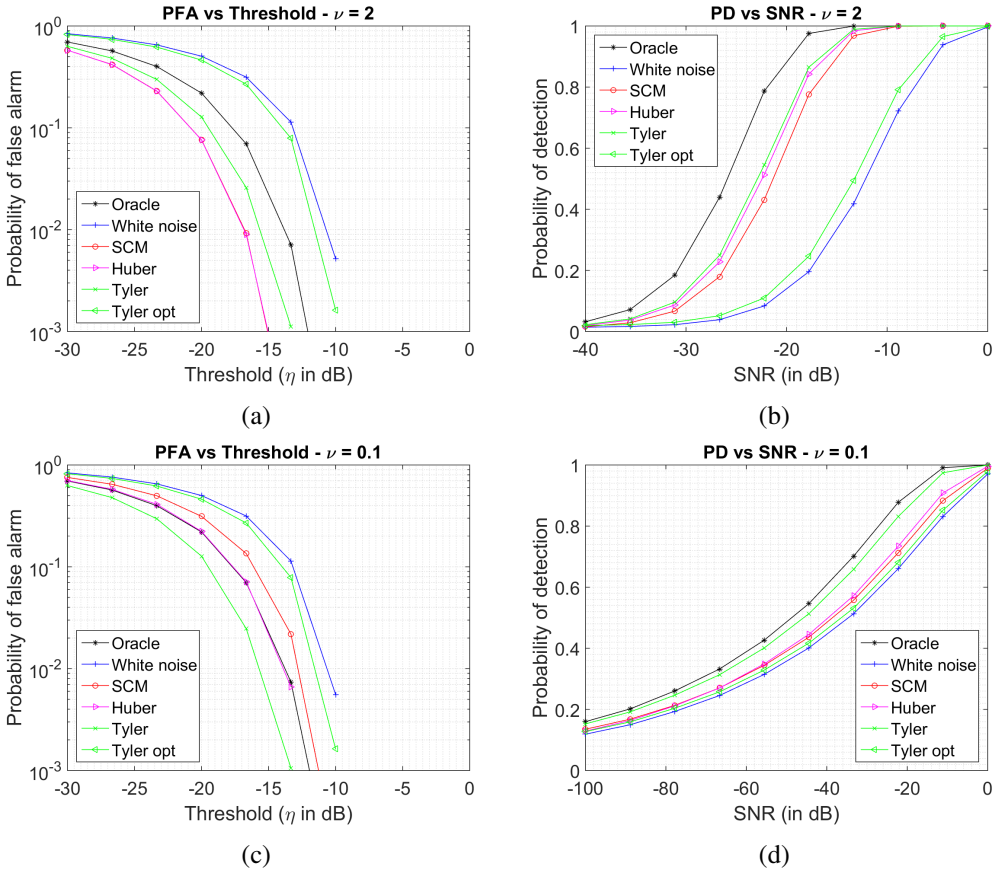

Figure 3: Performance graphs for estimators. (a) PFA versus Threshold ($\nu = 2$), (b) PD versus SNR ($\nu = 2$), (c) PFA versus Threshold ($\nu = 0.1$), (d) PD versus SNR ($\nu = 0.1$). $N = 153$, $K = 40$.

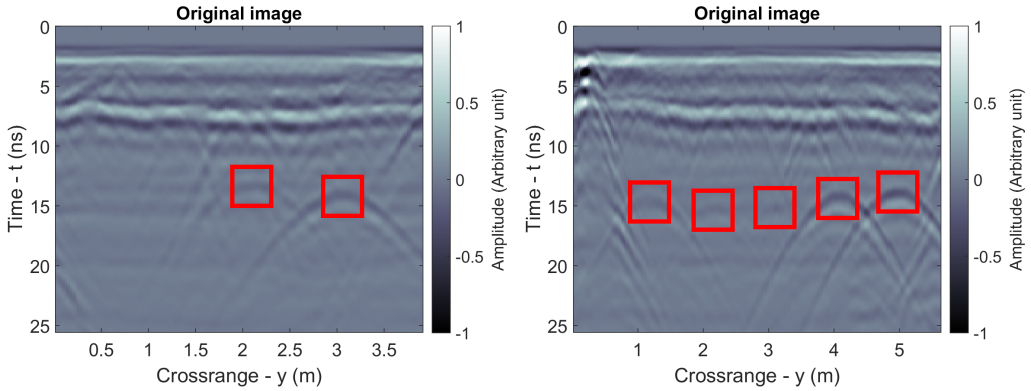

(a) 0039.RAD (b) 0028.RAD

Figure 4: Original test images. Approximate pipe locations are indicated by red squares.

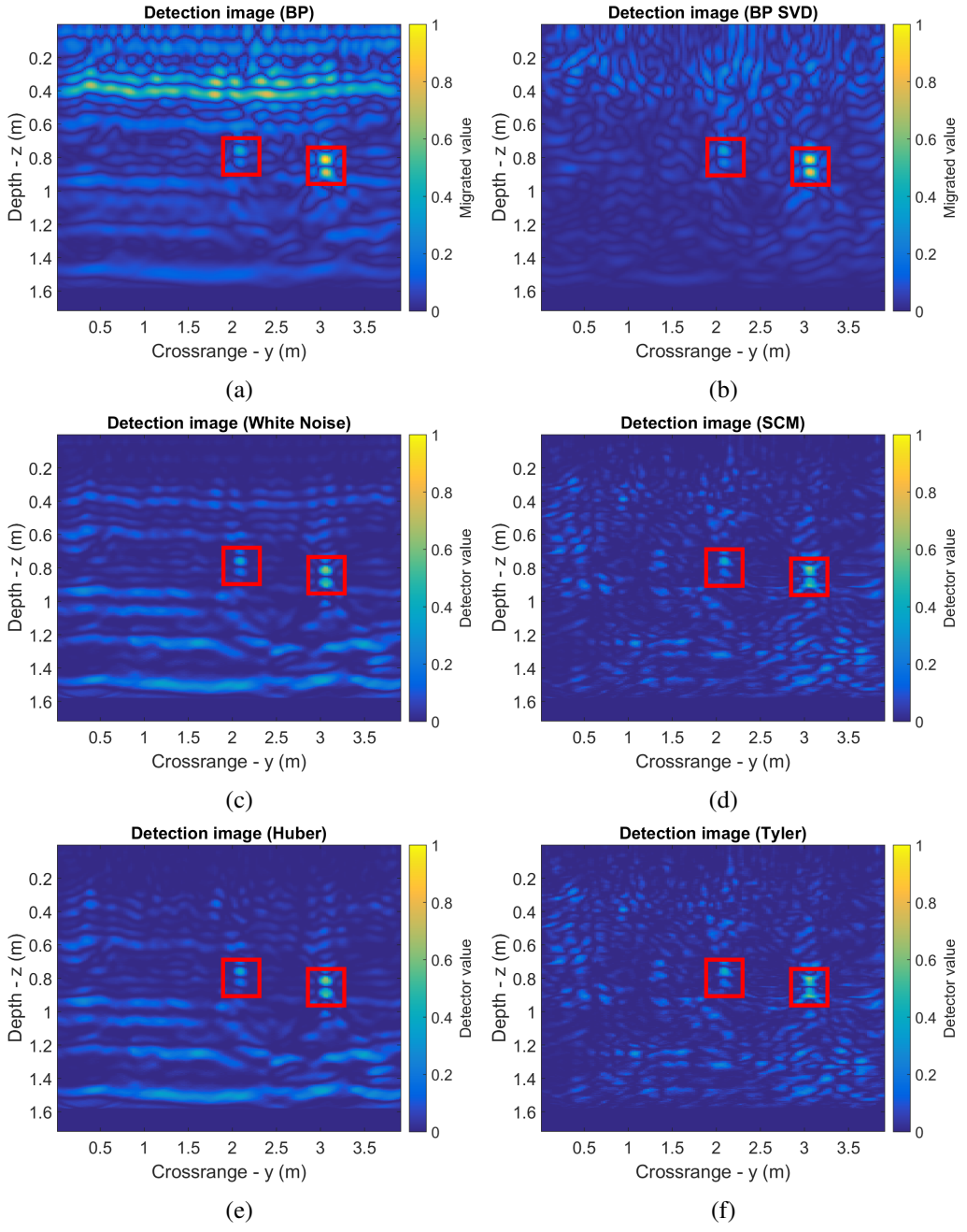

Figure 5: Adaptive detection for image 0039.RAD by using the following estimators: (a) Migration (b) Migration with preprocessing (c) White noise hypothesis (d) SCM (e) Huber (f) Tyler. $N = 153$, $K = 40$. Approximate pipe locations are indicated by red squares.

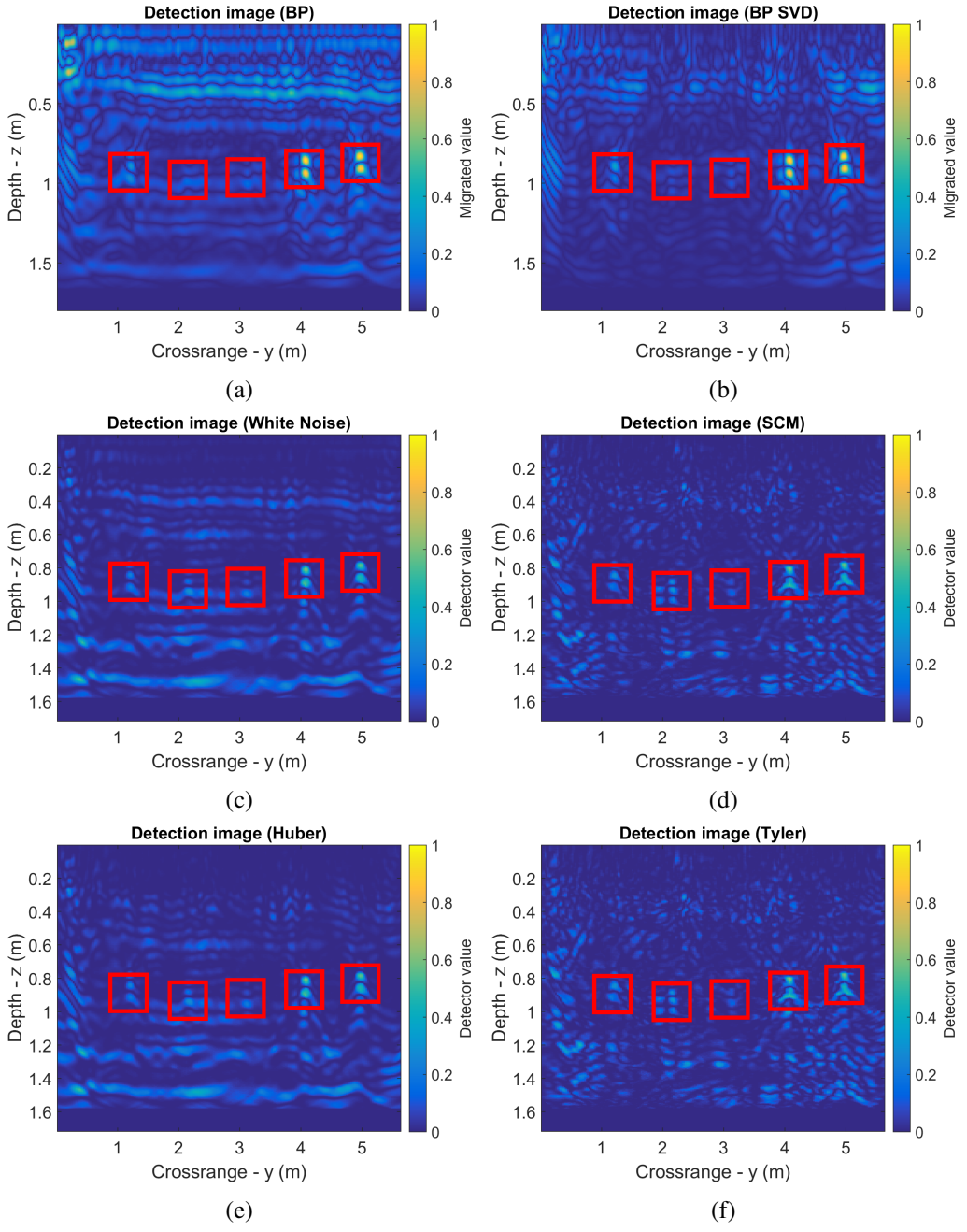

Figure 6: Adaptive detection for image 0028.RAD by using the following estimators: (a) Migration (b) Migration with preprocessing (c) White noise hypothesis (d) SCM (e) Huber (f) Tyler. $N = 153$, $K = 40$. Approximate pipe locations are indicated by red squares.

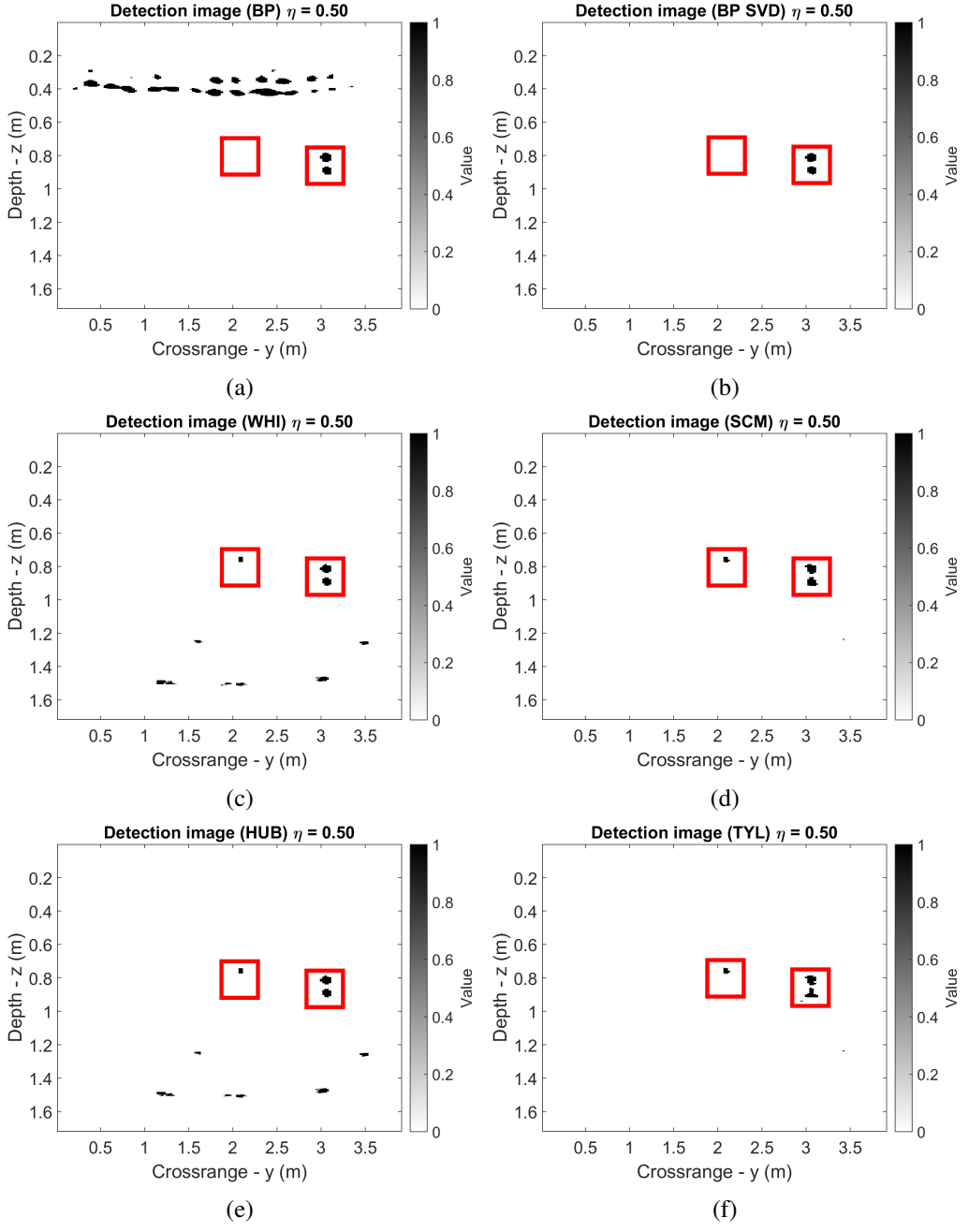

Figure 7: Image 0039.RAD: detection results of the proposed ANMFs as opposed to a standard migration. (a) Migration (b) Migration with preprocessing (c) White noise hypothesis (d) SCM (e) Huber (f) Tyler. Threshold is fixed at 50% of max value in each image. Approximate pipe locations are indicated by red squares.

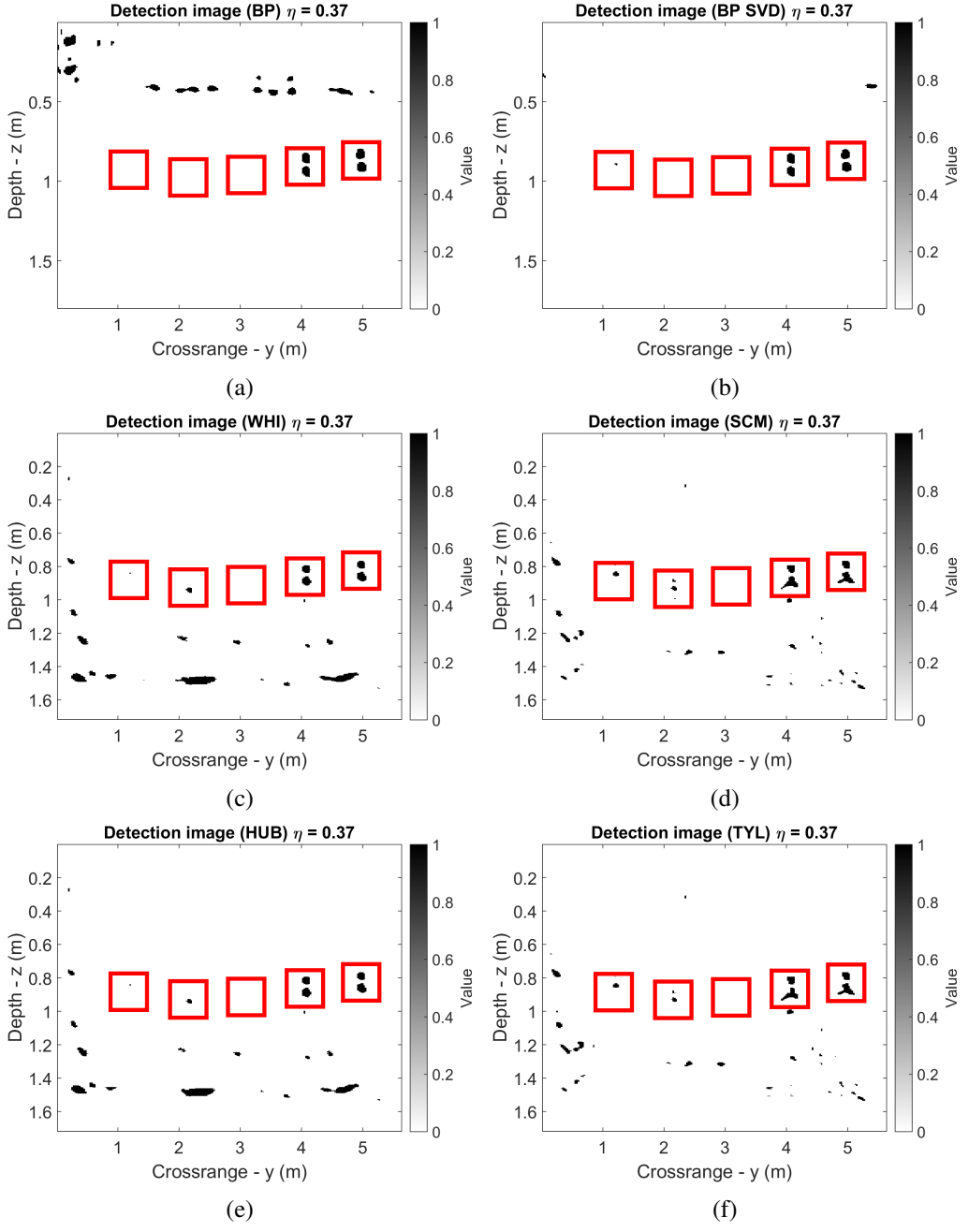

Figure 8: Image 0028.RAD: detection results of the proposed ANMFs as opposed to a standard migration. (a) Migration (b) Migration with preprocessing (c) White noise hypothesis (d) SCM (e) Huber (f) Tyler. Threshold is fixed at 37% of max value in each image. Approximate pipe locations are indicated by red squares.